Mon. Not. R. Astron. Soc. **376,** 180–192 (2007) doi:10.1111/j.1365-2966.2007.11399.x

Substructure in lensing clusters and simulations

Priyamvada Natarajan,[1,2]★ Gabriella De Lucia[3] and Volker Springel[3]

[1]*Department of Astronomy, Yale University, PO Box 208101, New Haven, CT 06511-208101, USA*
[2]*Department of Physics, Yale University, PO Box 208120, New Haven, CT 06511-208120, USA*
[3]*Max-Planck-Institut fur Astrophysik, Karl-Schwarzschild-Strasse 1, Postfach 1317, D-85748 Garching bei Munchen, Germany*

Accepted 2006 December 10. Received 2006 December 8; in original form 2006 April 11

ABSTRACT

We present high-resolution mass reconstructions for five massive cluster-lenses spanning a redshift range from $z = 0.18$ to 0.57 utilizing archival *Hubble Space Telescope* data and applying galaxy–galaxy lensing techniques. These detailed mass models were obtained from the observations by combining constraints from the strong and weak lensing regimes. We ascribe local weak distortions in the shear maps to perturbations induced by the presence of galaxy haloes around individual bright early-type cluster member galaxies. This technique constrains the mass enclosed within an aperture for these subhaloes. We are sensitive to a specific mass range for these subhaloes, 10^{11}–$10^{12.5}\,\mathrm{M}_{\odot}$, which we associate with galaxy-scale subhaloes. Adopting a parametric model for the subhaloes, we also derive their velocity dispersion function and the aperture radius function. The mass spectrum of substructure in the inner regions of the observed clusters is directly compared with that in simulated clusters extracted from the Millennium Simulation. The mass function, aperture radii and velocity dispersion function are compared in detail. Overall, we find good agreement between the distribution of substructure properties retrieved using the lensing analysis and those obtained from the simulation. We find that the fraction of total cluster mass associated with individual subhaloes within the inner 0.5–0.8 h^{-1} Mpc of our clusters ranges from 10–20 per cent, in broad agreement with simulations. Our work provides a powerful test of the Lambda cold dark matter model, which appears consistent with the amount of observed substructure in massive, lensing clusters based on the present data.

Key words: gravitational lensing – methods: numerical – galaxies: fundamental parameters – galaxies: haloes.

1 INTRODUCTION

Gravitational lensing has emerged as one of the most powerful techniques to map mass distributions on a range of scales: galaxies, clusters and beyond. The distortion in the shapes of background galaxies viewed through foreground mass distributions is independent of the dynamical state of the lens, therefore, compared with other methods for mass estimation there are fewer biases in lensing mass determinations. Here, we focus on mapping in detail the mass distribution inside the inner regions of massive clusters of galaxies using *Hubble Space Telescope* (*HST*) observations. We exploit the technique of galaxy–galaxy lensing, which was originally proposed as a method to constrain the masses and spatial extents of field galaxies (Brainerd, Blandford & Smail 1996), which we have since extended and developed over the years to apply inside clusters (Natarajan & Kneib 1997; Natarajan et al. 1998; Natarajan, Kneib & Smail 2002a).

The detailed mass distribution within clusters and specifically the fraction of the total cluster mass associated with individual galaxies has important implications for the frequency and nature of galaxy interactions in clusters (Richstone 1976; Farouki & Shapiro 1981; Merritt 1983; Moore et al. 1996; Ghigna et al. 1998; Okamoto & Habe 1999). Knowledge of the dynamical history of clusters enables a deeper understanding of the physical processes that shape their assembly and evolution. The discovery of strong evolution between $z \sim 0.5$ and the present day in the morphological (and star formation) properties of the galaxy populations in clusters has focused interest on environmental processes which could effect the gaseous component and dark matter halo of a cluster galaxy (e.g. Couch et al. 1998).

The global tidal field of a massive, dense cluster potential well is expected to be strong enough to truncate the dark matter halo of a galaxy whose orbit penetrates the cluster core. Therefore, probing the extents of galaxy haloes in clusters can provide invaluable clues

★E-mail: priya@astro.yale.edu

to dynamically dominant processes in clusters. For instance, the survival of individual, compact dark haloes associated with cluster galaxies suggests a high probability for galaxy–galaxy collisions within rich clusters over a Hubble time. However, since the internal velocity dispersions of cluster galaxies ($\lesssim 200\,\mathrm{km\,s^{-1}}$) are significantly lower than their orbital velocities, these interactions are, in general, unlikely to lead to mergers, but rather encounters of the kind simulated in the galaxy harassment picture by Moore et al. (1996, 1999).

Previous work on galaxy–galaxy lensing in the moderate redshift field has identified a signal associated with massive haloes around typical field galaxies, extending to beyond[1] 100 kpc (e.g. Brainerd et al. 1996; Hudson et al. 1998; Hoekstra, Yee & Gladders 2004; Ebbels et al., private communication). In particular, Hoekstra et al. (2004) report the detection of a finite truncation radius of 185 ± 30 kpc via weak lensing by galaxies based on imaging data from the Red-Sequence Cluster Survey. Galaxy–galaxy lensing results from the analysis of the Sloan Digital Sky Survey data (Guzik & Seljak 2002; McKay et al. 2002; Sheldon et al. 2004) have contributed to a deeper understanding of the relation between mass and light. Similar analysis of galaxies in the cores of rich clusters suggests that the average mass-to-light ratio (M/L) and spatial extent of the dark matter haloes associated with morphologically classified early-type galaxies in these regions may differ from those of field galaxies with comparable luminosity (Natarajan et al. 1998, 2002a). We find that at a given luminosity, galaxies in clusters have more compact halo sizes and lower masses (by a factor of 2–5) compared to their field counterparts. The M/L values inferred for cluster galaxies in the V band are also lower than those of field galaxies with comparable luminosity. This is a strong indication of the effect of the dense environment on the properties of dark matter haloes.

In this paper, we present a determination of the mass function and other detailed properties of substructure in clusters using galaxy–galaxy lensing techniques. A high-resolution mass model tightly constrained by strong and weak lensing observations is constructed including individual cluster galaxies and their associated dark matter haloes. These lensing models are new and incorporate recent observed spectroscopic redshifts of several additional multiple images. We show that over a limited mass range we can successfully construct the mass function of subhaloes inside clusters. In earlier work, we compared the mass function obtained from lensing with that extracted from a massive cluster simulated at extremely high resolution (Natarajan & Springel 2004). In this work, we are able to compare with a large ensemble of simulated clusters, significantly strengthening the statistical significance of our results.

N-body simulations represent an indispensable tool for investigating the non-linear growth of structures in its full geometrical complexity. The high numerical resolution achieved in recent years has demonstrated that the cores of dark matter haloes that fall into a larger system can survive for a relatively long time as self-gravitating objects orbiting in the smooth dark matter background of the system. A wealth of dark matter substructures is now routinely detected and studied with the aid of *N*-body simulations confirming that the existence of substructures is a generic prediction of hierarchical structure formation in cold dark matter (CDM) models.

The subhalo mass function (i.e. the abundance of dark matter substructure as a function of mass) represents an important prediction of hierarchical CDM structure formation models and has been subject of intense studies since the 'dwarf galaxy crisis' was identified (Klypin et al. 1999; Moore et al. 1999). Within a radius of $400\,h^{-1}$ kpc, from the Milky Way, cosmological models of structure formation predict $\sim$30 dark matter satellites with circular velocities in excess of $20\,\mathrm{km\,s^{-1}}$ and mass greater than $3 \times 10^8\,\mathrm{M}_\odot$. This number is significantly higher than the dozen or so satellites actually observed around our Galaxy. Different explanations have been suggested for this discrepancy. The missing satellites could for example be identified with the detected high velocity clouds (Maller & Bullock 2004). *Warm* or *self-interacting* dark matter could also selectively suppress power on the small scales, therefore reducing the predicted number of satellites (Spergel & Steinhardt 2000). The leading hypothesis however remains that the solution to this problem lies in astrophysical processes such as heating by a photoionizing background that suppresses star formation in small haloes at early times (Bullock, Kravtsov & Weinberg 2000; Benson et al. 2002; Kravtsov, Gnedin & Klypin 2004). On the scale of galaxy clusters, many more dark matter structures are expected to host visible galaxies, thus making the comparison with expectations from numerical simulations less affected by uncertainties in the physics of galaxy formation. Full consistency is to be expected here, therefore providing an important test of the CDM paradigm.

Our innovative application of gravitational lensing enables a mapping of the distribution in mass of dark matter substructure (subhalo mass function) therefore allowing a direct comparison with results from numerical simulations. The strength of the lensing analysis presented here derives from the combination of both strong and weak lensing features which are used together to construct a high-resolution mass map of a galaxy cluster. Anisotropies in the shear field (i.e. departure from the coherent tangential signal) in the vicinity of bright, early-type cluster members are attributed to the presence of these local potential wells. Statistically stacking this signal provides a way to quantify the masses associated with individual galaxy haloes. This is accomplished using a maximum likelihood estimator to retrieve characteristic properties for a typical subhalo in the cluster.

The comparison with clusters from the Millennium Simulation we use here is particular powerful due to the large volume and high resolution of this simulation. The simulation used more than 10 billion particles to trace the evolution of the dark matter distribution in a cubic region of the Universe over 2 billion light-years on a side. This makes it an ideal data set for comparison with lensing clusters, providing dozens of highly resolved, massive lensing clusters out to redshifts $z \simeq 0.6$ and beyond.

The outline of this paper is as follows. In Section 2, we describe briefly the formalism for analysing galaxy–galaxy lensing in observed clusters including a synopsis of the adopted models. Section 3 presents the best-fitting lens models and discusses the uncertainties and sources of error. A detailed comparison with clusters from the Millennium Simulation is presented in Section 4. The results of comparing the mass function of substructure, the distributions of aperture radii and the velocity dispersions are discussed. Finally, we conclude with a discussion of the implications of our results for the ΛCDM model and the future prospects of this work in Section 5.

2 GALAXY–GALAXY LENSING IN CLUSTERS

2.1 Framework for analysis

In this section, we briefly outline the analysis framework, noting that further details can be found in earlier papers (Natarajan & Kneib 1997; Natarajan et al. 1998). For the purpose of extracting the prop-

[1] We adopt $h = H_0/100\,\mathrm{km\,s^{-1}\,Mpc^{-1}} = 0.7$ and $\Omega_\Lambda = 0.7$, and scale other published results to this choice of parameters.

erties of the subhalo population in clusters, a range of mass scales is modelled parametrically. The X-ray surface brightness maps of clusters suggest the presence of a smooth, dominant, large-scale mass component. Clusters are therefore modelled as a superposition of a smooth large-scale potential and smaller scale potentials that are associated with bright early-type cluster members:

$$\phi_{\rm tot} = \phi_{\rm smooth} + \Sigma_i\, \phi_{\rm p_i}, \tag{1}$$

where $\phi_{\rm smooth}$ is the potential of the smooth component and $\phi_{\rm p_i}$ is the potential of the subhalo associated with the ith galaxy, and is treated as perturber. The amplification matrix A^{-1} can be decomposed into contributions from the main clump and the perturbers:

$$A^{-1} = (1 - \kappa_{\rm smooth} - \Sigma_i \kappa_{\rm p})\, I - \gamma_{\rm smooth} J_{2\theta_{\rm smooth}} - \Sigma_i\, \gamma_{\rm p_i} J_{2\theta_{\rm p_i}},$$

where κ is the magnification and γ the shear. The shear γ is in fact a complex number and is used to define the reduced shear $\overline{g}$, which is the quantity that is measured directly from the observed shapes of background galaxies. Similarly, the reduced shear can also be decomposed as

$$\overline{g_{\rm tot}} = \frac{\overline{\gamma}}{1-\kappa} = \frac{\overline{\gamma}_{\rm smooth} + \Sigma_i\, \overline{\gamma}_{p_i}}{1 - \kappa_{\rm smooth} - \Sigma_i\, \kappa_{p_i}}. \tag{2}$$

In the frame of an individual perturber j (and neglecting the effect of perturber i if $i \neq j$), this simplifies to

$$\overline{g}_{\rm tot}|_j = \frac{\overline{\gamma}_{\rm smooth} + \overline{\gamma}_{p_j}}{1 - \kappa_{\rm smooth} - \kappa_{p_j}}. \tag{3}$$

Restricting our analysis to the weak regime, and thereby retaining only the first-order terms from the lensing equation for the shape parameters (e.g. Kneib et al. 1996), we have

$$\overline{g}_{\rm I} = \overline{g}_{\rm S} + \overline{g}_{\rm tot}, \tag{4}$$

where $\overline{g}_{\rm I}$[2] is the distortion of the image, $\overline{g}_{\rm S}$ the intrinsic shape of the source, and $\overline{g}_{\rm tot}$ is the distortion induced by the lensing potentials.

In the local frame of reference of the perturbers, the mean value of the quantity $\overline{g}_{\rm I}$ and its dispersion can be computed in circular annuli (at radius r from the perturber centre) *strictly in the weak regime*, assuming a constant value $\gamma_{\rm c} e^{{\rm i}\theta_{\rm c}}$ for the smooth cluster component over the area of integration. In the frame of the perturber, the averaging procedure allows efficient subtraction of the large-scale component, enabling the extraction of the shear component induced in the background galaxies only by the local perturber. The background galaxies are assumed to have intrinsic ellipticities drawn from a known distribution (see the next section for further details). Schematically, the effect of the cluster on the intrinsic ellipticity distribution of background sources is to cause a coherent displacement τ and the presence of perturbers merely adds small-scale noise to the observed ellipticity distribution.

The feasibility and robustness of signal detection has been amply demonstrated in earlier papers by Natarajan et al. The primary limitations in this analysis arise from the total number of distorted background galaxies, and the accuracy with which the smooth cluster component can be constrained using multiple images in the inner region. The partition into this smooth component and its effective subtraction in fact boosts the shear induced by the perturber. In particular, the shear induced by the subhalo has a $(\kappa_{\rm smooth} + \kappa_{p_j})$ term in the denominator, which becomes non-negligible in the cluster centre. The subtraction of the larger scale component reduces the noise in the polarization measure by about a factor of two in cluster cores. This differenced averaging prescription for extracting the distortions induced by the possible presence of dark haloes around cluster galaxies is feasible with *HST* quality data as we have shown in earlier work (Natarajan et al. 1998, 2002a). The robustness of this technique also has been demonstrated in our earlier published work. Note here that it is the presence of the underlying large-scale smooth mass distribution (with a high value of $\kappa_{\rm c}$) that enables the extraction of the weak signal riding on it. It is instructive to keep in mind that, in the regimes of interest discussed here, the distortion induced by the cluster-scale smooth component for a pseudo-isothermal elliptical component model (PIEMD) in the innermost (with a velocity dispersion of $1000\,{\rm km\,s^{-1}}$ and at $R/r_{\rm t} \leqslant 0.1$) regions is typically of the order of 20–40 per cent or so in background galaxy shapes, and the perturbers produce distortions (smaller scale PIEMDs with a velocity dispersion of $220\,{\rm km\,s^{-1}}$) of the order of 5–10 per cent, significantly more than in the case of weak lensing by large-scale structure or cosmic shear, wherein the distortions are of the order of 1 per cent.

[2] The measured image shape and orientation are used to construct a complex number whose magnitude is given in terms of the semimajor axis (i) and semiminor axis (ii) of the image and the orientation is the phase of the complex number.

2.2 Modelling the cluster

Each of the clusters studied in this paper preferentially probes the high-mass end of the cluster mass function and has a surface mass density in the inner regions which is higher than the critical value, therefore producing a number of multiple images of background sources. By definition, the critical surface mass density for strong lensing is given by

$$\Sigma_{\rm crit} = \frac{c^2}{4\pi G} \frac{D_{\rm s}}{D_{\rm d} D_{\rm ds}}, \tag{5}$$

where $D_{\rm s}$ is the angular diameter distance between the observer and the source, $D_{\rm d}$ the angular diameter distance between the observer and the deflecting lens, and $D_{\rm ds}$ the angular diameter distance between the deflector and the source. When the surface mass density in the cluster is in excess of this critical value, strong-lensing phenomena with high magnification are observed.

In general two types of lensing effects are produced – strong: multiple images and highly distorted arcs; and weak: small distortions in background image shapes determined by the criticality of the region. Viewed through the central, dense core region of the mass distribution, where $\kappa > 1$ strongly lensed features are observed. Note that the integrated lensing signal detected is due to all the mass distributed along the line of sight in a cylinder projected on to the lens plane. In this and all other cluster-lensing work, the assumption is made that individual clusters dominate the lensing signal as the probability of encountering two massive rich clusters along the same line of sight is extremely small due to the fact that these are very rare objects in hierarchical structure formation models.

With our current sensitivity limits, galaxy–galaxy lensing within the cluster is primarily a tool to determine the total enclosed mass within an aperture. We lack sufficient sensitivity to constrain the detailed mass profile for individual cluster galaxies. With higher resolution data in the near future we will be able to obtain constraints on the slopes of mass profiles in subhaloes. In this paper, we therefore concentrate on pseudo-isothermal elliptical components (PIEMD models, derived by Kassiola & Kovner 1993) appropriately scaled for both the main cluster and the substructures. Some of the cluster studied in this work are bimodal (i.e. have two significant, large-scale mass peaks), therefore, when required we employ two large-scale smooth potentials and a superposition of subhaloes. We

find that the results obtained for the characteristics of the subhaloes (or perturbers) is largely independent of the form of the mass distribution (the aperture mass is comparable for the NFW and PIEMD models) used to model the smooth, large-scale component.

To quantify the lensing distortion induced by the global potential, both the smooth and individual galaxy-scale haloes are modelled self-similarly using a surface density profile, $\Sigma(R)$, which is a linear superposition of two PIEMD distributions,

$$\Sigma(R) = \frac{\Sigma_0 r_0}{1 - r_0/r_{\rm t}} \left(\frac{1}{\sqrt{r_0^2 + R^2}} - \frac{1}{\sqrt{r_{\rm t}^2 + R^2}} \right), \tag{6}$$

with a model core-radius r_0 and a truncation radius $r_{\rm t} \gg r_0$. These parameters $(r_{\rm t}, r_0)$ are tuned for both the smooth component and the perturbers to obtain mass distributions on the relevant scales. The coordinate R is a function of x, y and the ellipticity,

$$R^2 = \frac{x^2}{(1+\epsilon)^2} + \frac{y^2}{(1-\epsilon)^2}, \quad \text{where} \quad \epsilon = \frac{a-b}{a+b}. \tag{7}$$

The mass enclosed within radius R for the $\epsilon = 0$ model is given by

$$M(R) = \frac{2\pi\Sigma_0 r_0}{1 - r_0/r_{\rm t}} \left[\sqrt{r_0^2 + R^2} - \sqrt{r_{\rm t}^2 + R^2} + (r_{\rm t} - r_0) \right]. \tag{8}$$

One of the attractive features of this model is that the total mass M is finite, $M \propto \Sigma_0 r_0 r_{\rm t}$. Besides, analytic expressions can be obtained for the all the quantities of interest, κ, γ and g, for example,

$$\kappa(R) = \kappa_0 \frac{r_0}{1 - r_0/r_{\rm t}} \left(\frac{1}{\sqrt{r_0^2 + R^2}} - \frac{1}{\sqrt{r_{\rm t}^2 + R^2}} \right), \tag{9}$$

$$2\kappa_0 = \Sigma_0 \frac{4\pi G}{c^2} \frac{D_{\rm ls} D_{\rm ol}}{D_{\rm os}}, \tag{10}$$

where $D_{\rm ls}$, $D_{\rm os}$ and $D_{\rm ol}$ are the lens–source, observer–source and observer–lens angular diameter distances, respectively, which do depend on the choice of cosmological parameters. To obtain $g(R)$ knowing the magnification $\kappa(R)$, we solve Laplace's equation for the projected potential $\phi_{\rm 2D}$, evaluate the components of the amplification matrix and then proceed to solve directly for $\gamma(R)$, and then $g(R)$:

$$\gamma(R) = \kappa_0 \left[-\frac{1}{\sqrt{R^2 + r_0^2}} + \frac{2}{R^2}\left(\sqrt{R^2 + r_0^2} - r_0 \right) + \frac{1}{\sqrt{R^2 + r_{\rm t}^2}} - \frac{2}{R^2}\left(\sqrt{R^2 + r_{\rm t}^2} - r_{\rm t} \right) \right]. \tag{11}$$

Scaling this relation by $r_{\rm t}$ gives for $r_0 < R < r_{\rm t}$:

$$\gamma(R/r_{\rm t}) \propto \frac{\Sigma_0}{\eta - 1} \frac{r_{\rm t}}{R} \sim \frac{\sigma^2}{R}, \tag{12}$$

where σ is the velocity dispersion and for $r_0 < r_{\rm t} < R$:

$$\gamma(R/r_{\rm t}) \propto \frac{\Sigma_0}{\eta} \frac{{r_{\rm t}}^2}{R^2} \sim \frac{M_{\rm tot}}{R^2}, \tag{13}$$

where $M_{\rm tot}$ is the total mass. In the limit that $R \gg r_{\rm t}$, we have

$$\gamma(R) = \frac{3\kappa_0}{2R^3}\left(r_0^2 - r_{\rm t}^2 \right) + \frac{2\kappa_0}{R^2}(r_{\rm t} - r_0), \tag{14}$$

and as $R \to \infty, \gamma(R) \to 0, g(R) \to 0$ and $\tau(R) \to 0$, as expected.

It is further assumed that the ellipticity and the orientation of the dark matter subhaloes associated with the early-type cluster members are identical to that of the galaxies themselves. Additionally, in order to relate the light distribution to key parameters of the mass model above, we adopt a set of physically motivated scaling laws for the cluster galaxies (Brainerd et al. 1996):

$$\sigma_0 = \sigma_{0*}\left(\frac{L}{L^*} \right)^{1/4}, \; r_0 = r_{0*}\left(\frac{L}{L^*} \right)^{1/2}, \; r_{\rm t} = r_{t*}\left(\frac{L}{L^*} \right)^{\alpha}. \tag{15}$$

These in turn imply the following scaling for the $r_{\rm t}/r_0$ ratio η:

$$\eta = \frac{r_{\rm t}}{r_0} = \frac{r_{t*}}{r_{0*}} \left(\frac{L}{L^*} \right)^{\alpha - 1/2}. \tag{16}$$

The total mass $M_{\rm ap}$ enclosed within an aperture r_{t*} and the total M/L then scale with the luminosity as follows:

$$M_{\rm ap} \propto \sigma_{0*}^2 r_{t*} \left(\frac{L}{L^*} \right)^{1/2+\alpha}, \; M/L \propto \sigma_{0*}^2 r_{t*} \left(\frac{L}{L^*} \right)^{\alpha - 1/2}, \tag{17}$$

where α determines the size of the galaxy halo. For $\alpha = 0.5$ the assumed galaxy model has constant M/L with luminosity (but not as a function of radius) for each galaxy. We adopt $\alpha = 0.5$ throughout this work, as this scaling is empirically motivated by the Faber–Jackson relation for early-type galaxies (Brainerd et al. 1996). We assume these scaling relations and recognize that this could ultimately be a limitation of our model but the evidence at hand supports the fact that mass traces light efficiently both on cluster scales (Kneib et al. 2003) and on galaxy scales (Wilson et al. 2001; McKay et al. 2002). The calibration factors σ_{0*} and r_{t*} in equation (15) are provided by the results of a likelihood method discussed further in Section 2.3.

2.2.1 *The intrinsic shape distribution of background galaxies*

As in all lensing work, it is assumed here as well that the intrinsic or undistorted distribution of shapes of background galaxies is known. This distribution is obtained from shape measurements taken from deep images of blank field surveys. Previous analysis of deep survey data such as the MDS fields (Griffiths et al. 1994) showed that the ellipticity distribution of sources is a strong function of the sizes of individual galaxies as well as of their magnitude (Kneib et al. 1996). For the purposes of our modelling, the intrinsic ellipticities for background galaxies are assigned in concordance with an ellipticity distribution $p(\tau_{\rm S})$ where the shape parameter τ is defined as $\tau = (a^2 - b^2)/(2ab)$ derived from the observed ellipticities of the CFHT12k data (see Limousin, Kneib & Natarajan 2005, for details):

$$p(\tau_{\rm S}) = \tau_{\rm S} \exp\left[-\left(\frac{\tau_{\rm S}}{\delta} \right)^{\nu} \right]; \; \nu = 1.15, \; \delta = 0.25. \tag{18}$$

Note that this distribution includes accurately measured shapes of galaxies of all morphological types. In the likelihood analysis this distribution $p(\tau_{\rm S})$ is the assumed prior, which is used to compare with the observed shapes once the effects of the assumed mass model are removed from the background images. We note here that the exact shape of the ellipticity distribution, that is, the functional form and the value of δ and ν do not change the results, but alter the confidence levels we obtain. The width of the intrinsic ellipticity distribution on the other hand is the fundamental limiting factor in the accuracy of all lensing measurements.

2.2.2 *The redshift distribution of background galaxies*

While the shapes of lensed background galaxies can be measured directly and reliably by extracting the second moment of the light distribution, the precise redshift for each weakly object is in general unknown and therefore needs to be assumed. Using multiwaveband data from surveys such as COMBO-17 (Wolf et al. 2004),

photometric redshift estimates can be obtained for every background object. Typically the redshift distribution of background galaxies is modelled as a function of observed magnitude $P(z, m)$. We have used data from the high-redshift survey VIMOS VLT Deep Survey (Le Fevre et al. 2004) as well as recent CFHT12k R-band data to define the number counts of galaxies, and the HDF prescription for the mean redshift per magnitude bin, and find that the simple parametrization of the redshift distribution used by Brainerd et al. (1996) still provides a good description to the data.

For the normalized redshift distribution at a given magnitude m (in the given band) we therefore have

$$N(z)|_m = \frac{\beta \left(z^2/z_0^2\right) \exp\left[-(z/z_0)^\beta\right]}{\Gamma\,(3/\beta)\; z_0}, \tag{19}$$

where $\beta = 1.5$ and

$$z_0 = 0.7 \left[z_{\rm median} + \frac{{\rm d}z_{\rm median}}{{\rm d}m_R}(m_R - m_{R0}) \right], \tag{20}$$

with $z_{\rm median}$ being the median redshift, and ${\rm d}z_{\rm median}/{\rm d}m_R$ being the change in median redshift with say the R-band magnitude, m_R.

However, we note here in agreement with another recent study of galaxy–galaxy lensing in the field by Kleinheinrich et al. (2005), that the final results for the aperture mass presented here are primarily sensitive to the choice of the median redshift of the distribution rather than the individual assigned values.

2.3 The maximum-likelihood method

There are two key aspects to constructing a successful lens model for the clusters analysed here. First, we must identify multiple-imaged background sources with reliable redshift measurements whose properties can be used to constrain the total projected mass within the Einstein radius. The strong-lensing observations provide constraints in the inner regions for the global smooth potential. Secondly, we use the weak shear detected out to larger radii to constrain the behaviour of the smooth component and simultaneously statistically constrain the properties of the subhaloes. This is done by quantifying the anisotropies that arise in the shear field and attributing these anisotropies to the presence finite mass subhaloes.

Parameters that characterize both the global component and the perturbers are optimized, using the observed strong-lensing features – positions, magnitudes, geometry of multiple images and measured spectroscopic redshifts, when known, along with the smoothed shear field as constraints. As initial values of the mass model we provide a centre, velocity dispersion, ellipticity, orientation and truncation radius for the main clump with tolerance ranges. For the subhaloes, we provide the locations (coincident with the positions of the selected early-type cluster members), ellipticity and orientation (taken from measurements for the cluster early-types). In combination with the parametrization presented in the previous section, we then optimize and extract values for the central velocity dispersion and the aperture scale (σ_{0*}, r_{t*}) for a typical L^* cluster galaxy.

A maximum-likelihood estimator is used to obtain significance bounds on fiducial parameters that characterize a typical L^* subhalo in the cluster. We have extended the prescription proposed by Schneider & Rix (1997) for galaxy–galaxy lensing in the field to the case of lensing by galaxy subhaloes in the cluster (Natarajan & Kneib 1997; Natarajan et al. 1998). The likelihood function of the estimated probability distribution of the source ellipticities is maximized for a set of model parameters, given a functional form of the intrinsic ellipticity distribution measured for faint galaxies. For each 'faint' galaxy j, with measured shape $\tau_{\rm obs}$, the intrinsic shape τ_{S_j} is estimated in the weak regime by subtracting the lensing distortion induced by the smooth cluster model and the galaxy subhaloes,

$$\tau_{S_j} = \tau_{\rm obs_j} - \Sigma_i^{N_{\rm c}}\, \gamma_{p_i} - \gamma_{\rm c}, \tag{21}$$

where $\Sigma_i^{N_{\rm c}} \gamma_{p_i}$ is the sum of the shear contribution at a given position j from $N_{\rm c}$ perturbers. This entire inversion procedure is performed numerically using code that builds on the ray-tracing routine LENSTOOL written by Kneib (1993). This machinery accurately takes into account the non-linearities arising in the strong-lensing regime. Using a well-determined 'strong-lensing' model for the inner regions of the clusters derived from the positions, shapes and magnitudes of the highly distorted multiple-imaged objects along with the shear field determined from the shapes of the weakly distorted background galaxies and assuming a known functional form for $p(\tau_S)$, the probability distribution for the intrinsic shape distribution of galaxies in the field, the likelihood for a guessed model is given by

$$\mathcal{L}(\sigma_{0*}, r_{t*}) = \Pi_j^{N_{\rm gal}}\, p(\tau_{S_j}), \tag{22}$$

where the marginalization is done over (σ_{0*}, r_{t*}). We compute $\mathcal{L}$ assigning the median redshift corresponding to the observed source magnitude for each arclet. The best-fitting model parameters are then obtained by maximizing the log-likelihood function with respect to the parameters σ_{0*} and r_{t*}. Note that the parameters that characterize the smooth component are also simultaneously optimized. The likelihood can also be marginalized over a complementary pair of parameters, for example, using the luminosity scaling index α and the aperture mass $M_{\rm ap}$ directly. In this work, we explore both choices.

3 BEST-FITTING LENSING MASS MODELS

A composite mass model is constructed for the clusters starting with the superposed PIEMDs. The strong-lensing data, that is, the geometry, positions, relative brightness, redshifts and parities of the multiple images are used to obtain the mass enclosed within the Einstein radius which is used as an initial constraint for the integrated mass in the inner regions. The contribution to the shear and magnification from all potentials (large-scale and small-scale perturbers) is calculated at the location of every observed background source galaxy and the inversion of the lensing equation is performed. The observed shape and magnification of each and every distorted background galaxy is compared to that computed from the model and the subhalo mass distribution is modified iteratively until the best match between the observations and the model is found simultaneously for all background sources. Strong-lensing constraints principally drive the likelihood results. Therefore, we use many sets of multiple images with measured redshifts for each cluster as inputs. Compared to our earlier work (Natarajan et al. 2002b) the models presented here have several improvements, we have incorporated more multiple image families with redshifts that have since become available and we have also modified the algorithm to enable finer grid searching. In our analysis, the centre of the cluster is picked to coincide with the location of the brightest cluster galaxy.

The basic steps of our analysis involve lens inversion, modelling and optimization, which are done using the LENSTOOL software utilities (Kneib 1993). These utilities are used to perform the ray tracing from the image plane to the source plane with a specified intervening lens. This is achieved by solving the lens equation iteratively, taking into account the observed strong-lensing features, positions, geometries and magnitudes of the multiple images. In some cases, we also include a constraint on the location of the critical line to

tighten the optimization. Additionally, we fix the core radius of an L^* subhalo to be 0.1 kpc, as by construction our analysis cannot constrain this quantity. In addition to the likelihood contours, the reduced χ^2 for the best-fitting model is also robust. We describe some pertinent features of each cluster and their respective mass models below.

A 2218: Our best-fitting mass model for the cluster is bimodal, composed of two large-scale clumps around the cD and the second brightest cluster galaxy. This model is an updated version of that constructed by Kneib et al. (1996). It includes 40 additional small-scale clumps that we associate with luminous early-type galaxies in the cluster core. Only about 10 per cent of the total cluster mass is in substructures, that is, associated with galaxy-scale haloes. The aperture mass, integrated over the truncation radius $r_{\rm ap} = 40$ kpc, yields a characteristic mass of $1.4 \times 10^{12}\,{\rm M}_{\odot}$, with a total M/L in the V band of $\sim 5.8 \pm 1.5$ and a central velocity dispersion of about $180\,{\rm km\,s^{-1}}$.

A 2390: The cluster has an unusual feature – a strongly lensed almost 'straight arc' (Pello et al. 1999) approximately 38 arcsec ($\sim$170 kpc) away from the central galaxy, in addition to many other arcs and arclets that have been utilized in our modelling. We find a best-fitting mass model with two large-scale components, that yield a projected mass within the radius defined by the brightest arc of $\sim 1.8 \pm 0.2 \times 10^{14}\,{\rm M}_{\odot}$. Our best-fitting composite lensing model for A 2390 incorporates 40 perturbers associated with early-type cluster members whose characteristic parameters are optimized in the maximum-likelihood analysis. The integrated mass within the $\sim$18 kpc tidal radius for a typical L^* cluster galaxy is about $6.4 \times 10^{11}\,{\rm M}_{\odot}$ giving a total M/L in the V band of about 4.2 ± 1.3. Again, 90 per cent of the total mass of the cluster is consistent with being smoothly distributed.

Cl 2244–02: The best-fitting lens model for this cluster has two components which both have fairly low-velocity dispersions. This is the least massive lensing cluster in the sample studied here. The X-ray mass estimate from the *ASCA* data (Ota, Mitsuda & Fukazawa 1998) is in good agreement with our best-fitting lensing mass model. This is despite the fact that the X-ray temperature of Cl 2244–02 is at least a factor of 2 higher than that expected from the average luminosity–temperature relation.

The tidal truncation radius obtained for a typical L^* cluster galaxy in Cl 2244 is the largest in the sample studied here and is 55 ± 12 kpc. This is consistent with the fact that the central density in Cl 2244 is the lowest. The total M/L in the V band for a fiducial L^* is 3.2 ± 1.2. Approximately 20 per cent of the total mass is in substructure within the mass range 10^{11}–$10^{12.5}\,{\rm M}_{\odot}$.

Cl 0024+16: Our best-fitting mass model for the inner regions takes into account the small scale dark haloes associated with the early-type members in the core, and requires a two component model for the subclusters. Integrating the best-fitting mass model shown, we find that (i) about 10 per cent of the total cluster mass is in galaxy-scale haloes and (ii) the total mass estimate is in good agreement with that obtained by Kneib et al. (2003) where data from a much larger field of view were used.

Even on the large scales probed by Kneib et al. (2003) it was found that mass and light traced each other rather well at large radii. A typical L^* cluster galaxy was found to have a truncation radius of 45 ± 5 kpc, and a central velocity dispersion of $125 \pm 7\,{\rm km\,s^{-1}}$.

Cl 0054–27: The lensing signal from Cl 0054–27 is best fitted by a single smooth dark matter component and subhaloes associated with bright, early-type members making it the only unimodal cluster in the sample studied here. The mass enclosed within $\sim$400 kpc is of the order of $1.8 \pm 0.4 \times 10^{14}\,{\rm M}_{\odot}$.

The characteristic central velocity dispersion of a typical L^* galaxy in this cluster is higher than in A 2218, A 2390 or Cl 0024+16, all of which are by contrast bimodal in the mass distribution. In this cluster, about 20 per cent of the total mass is in substructure. However, Cl 0054−27 is the most distant cluster studied here and is likely to be still evolving and assembling, accounting for the high-mass fraction in substructure.

Note here that the choice of α determines only the scaling of the outer radius of a fiducial subhalo with luminosity. With the data used in this paper it is not possible to distinguish between various values of α – some values are clearly more physical than others. Therefore, this implies that we are sensitive to the integrated mass within an aperture that is determined primarily by the anisotropy in the shear field and not by the details of how the subhalo masses are truncated. We also find that out to 500 kpc in all clusters only 10–20 per cent of the total mass is associated with galaxy haloes. At this radius (to which we are limited due to the size of the *HST* WFPC2 fields), most of the mass is in the large-scale component. This fraction is likely to be a strong function of cluster-centric radius. The dependence of these aperture radii with distance from the cluster can be explored with wide-field *HST* data and we are in the process of doing so for the cluster Cl 0024+16 (Natarajan et al., in preparation).

3.1 Results from the lens models

We successfully construct high-resolution mass models for all five clusters from the unambiguous galaxy–galaxy lensing signal detected using the maximum-likelihood analysis. We constrain the mass enclosed within an aperture for a fiducial halo. The maximum-likelihood analysis yields the following: (i) the M/L in the V band of a typical L^* galaxy does not evolve significantly as a function of redshift, (ii) the fiducial truncation radius of an L^* galaxy varies

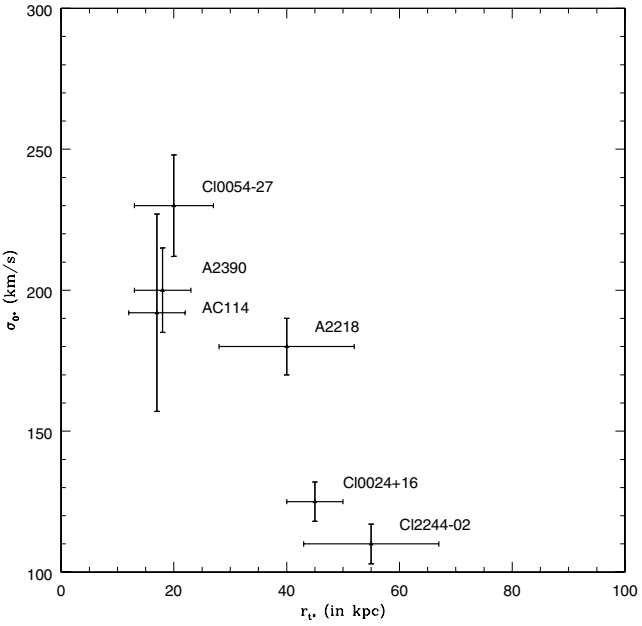

Figure 1. The retrieved best-fitting values for the two parameters that were marginalized over in the likelihood analysis, the central velocity dispersion and aperture radius for an L^* galaxy in each of the clusters. Included is the previously published data point for AC114. The error bars are 3σ for both σ_{0*} and r_{t*}. It is these error bars that translate into a factor of 2 error in the total aperture mass.

Table 1. Properties for the primary and (where relevant) secondary mass clumps in the clusters. The characteristic parameters are initially constrained by the positions, shapes and luminosities of the multiple-imaged objects and are then iteratively varied to match the weak shear field as well to obtain the optimal values (in the χ^2 sense) in a likelihood scheme.

z	x (arcsec)	y (arcsec)	ϵ	θ (°)	σ (km s^{-1})	r_t (kpc)	r_c (kpc)
A 2218							
0.17	0.5	1.2	0.2	−17	1100	900	65
0.17	−65.5	3.0	0.2	18	430	600	20
A 2390							
0.23	0.0	0.0	0.1	17	1040	900	50
0.23	−0.04	−2.70	0.3	18	470	60	15
Cl 2244−02							
0.33	0.0	0.0	0.17	45	680	900	30
0.33	17.32	−10.2	0.15	80	340	600	20
Cl 0024+16							
0.39	0.3	1.6	0.3	−10	1030	900	25
0.39	1.78	73.3	0.3	40	240	200	15
Cl 0054−27							
0.57	0.0	−1.0	0.2	−22	1100	900	30

from about 20–70 kpc depending on the cluster (iii) the typical central velocity dispersion is roughly 180 km s^{-1}. In Fig. 1, we show the recovered parameters (σ_{0*}, r_{t*}) for an L^* galaxy from the maximum-likelihood analysis. For the galaxy mass model adopted in our analysis, the total mass of an L^* galaxy varies from $\sim 4.9 \times 10^{11}$ to $1.4 \times 10^{12}\,\mathrm{M}_\odot$. We note that the distribution of these recovered parameters points to roughly two kinds of typical haloes, compact, dense ones and more extended ones. However, given that these lensing clusters do not constitute a well defined sample it is premature to claim any dichotomy. The M/L values obtained take passive evolution of elliptical galaxies into account as given by the stellar population synthesis models of Bruzual & Charlot (2003), therefore any detected trend reflects pure mass evolution. The mass obtained for a typical bright cluster galaxy by Tyson, Kochanski & De'll Antonio (1998) using only strong-lensing constraints inside the Einstein radius of the cluster Cl 0024+1654, at $z = 0.41$, is consistent with our results. All error bars quoted here are $\sim 3\sigma$. All best-fitting model parameters are presented in Table 1.

By construction, the maximum-likelihood technique presented here provides the mass spectrum of subhaloes in the cluster directly. Note that as stated before, in performing the likelihood analysis to obtain characteristic parameters for the subhaloes in the cluster, it is assumed that light traces mass. This is an assumption that is well supported by galaxy–galaxy lensing studies in the field (Wilson et al. 2001) as well as in clusters (Clowe & Scheider 2002). In fact, all lens modelling and rotation curve measurements suggest an excess of baryons in the inner regions. Note however that for our choice of mass model (the PIEMD) the M/L is not constant with radius within an individual galaxy halo. Since the procedure involves a scaled, self-similar mass model that is parametric, we obtain a mass estimate for the dark haloes (subhaloes) as a function of the luminosity of the early-type galaxy hosted by them. This provides us with a clump mass spectrum. We surmise that truncation by the cluster causes these galaxy halo masses to be lower than that of equivalent luminosity field galaxies at comparable redshifts obtained from galaxy–galaxy lensing. The fraction of mass in these clumps is only 10–20 per cent of the total mass of the cluster within the inner $500\,h^{-1}$ kpc of these high central density clusters. The remaining 80–90 per cent of the cluster mass is consistent with being smoothly distributed (in clumps with mass $M < 10^{10}\,\mathrm{M}_\odot$, the precise composition of this component depends on the hitherto unknown nature of dark matter. Note that the upper and lower limits on the mass spectrum vary from cluster to cluster due to the difference in the luminosity functions of cluster galaxies. These mass functions and other detailed properties of the substructure can now be directly compared to the subhalo mass functions of dark matter haloes taken from the Millennium Simulation, the results of which are presented in Section 4.

3.1.1 Uncertainties, sources of error and robustness of the lens models

The following tests were performed for each cluster: (i) choosing random locations (instead of bright, early-type cluster member locations) for the perturbers; (ii) scrambling the shapes of background galaxies; (iii) choosing to associate the perturbers with the 40 faintest (as opposed to the 40 brightest) galaxies; (iv) randomly selecting known cluster galaxies as perturbers and (v) selecting late-type galaxies. None of the above cases (i)–(v) yields a convergent likelihood map, in fact all that is seen in the resultant 2D likelihood surfaces is noise. We averaged the shear field in four radial bins around each cluster galaxy and stacked for each cluster to estimate the aperture mass within those bins. We found that the mean value of the shear in the innermost radial bin was $\sim 8 \pm 2$ per cent falling off to $\sim$2 per cent in the last radial bin indicating the presence of an aperture mass ranging from 10^{11}–$10^{12}\,\mathrm{M}_\odot$. Choosing random locations in the cluster (i.e. not the locations of early-type cluster members) we do not detect a shear profile in the stacked, direct averaging. Alternatively, we also used the locations of late-type galaxies (morphological classification from *HST* data is available for all the clusters studied here), to perform the direct averaging and did not detect any shear.

The robustness of our results has been extensively tested, however there are a couple of caveats that we ought to mention. As outlined above, in this galaxy–galaxy lensing technique we are only sensitive to a restricted mass range in terms of secure detection of substructure. This is due to the fact that we are quantifying a differential signal above the average tangential shear induced by a cluster, and we are inherently limited on by the average number of distorted background galaxies that lie within the aperture scale radii of cluster galaxies. This trade-off between requiring a sufficient number of lensed background galaxies in the vicinity of the subhaloes and the optimum locations for the subhaloes leads us to choose the brightest 40 early-type cluster galaxies for each lens. With deeper, wider and more numerous images of clusters, expected in the future with a wide-field imager in space such as the SNAP mission (Aldering et al. 2003), this technique can be pushed much further to probe down to lower masses in the mass function. It is possible that the bulk of the mass in subhaloes is in lower mass clumps (which in this analysis is essentially accounted for as part of the smooth component) and are in fact anticorrelated with positions of early-type galaxies.

Our results still hold true since we are filtering out only the most massive clumps via this technique. Note that one of the null tests performed above, associating galaxy haloes with random positions in the cluster (and not with the locations of bright, early-type galaxies) resulted in pure noise with an average value of the measured tangential shear ranging from −0.10 to 0.05. Even if we suppose that the bulk of the dark matter is associated with say, dwarf/very low surface brightness galaxies in clusters, then the spatial distribution of these galaxies is required to be fine-tuned such that these effects do not show up in the shear field in the inner re-

gions, implying that if at all they are likely to be more significant repositories of mass perhaps in the outskirts of clusters.

Guided by the current theoretical understanding of the assembly of clusters, dwarf galaxies are unlikely to survive in the high density core regions of galaxy clusters studied here. Studies such as the one presented here when applied on larger scales to distances of a few Mpc from the cluster centre will enable an understanding of the role of environment in mass stripping of these haloes. In a recent study, Limousin et al. (2006) track the mass inferred for a fiducial cluster galaxy as a function of cluster-centric distance out to twice the virial radius. Using ground-based data they do not detect any significant variation in mass, however, using mosaicked *HST* images Natarajan et al. (in preparation), find that a typical L^* galaxy halo has higher aperture mass in the outskirts of the cluster.

The principal sources of error in the above analysis are (i) shot-noise – we are inherently limited by the finite number of sources sampled within a few tidal radii of each cluster galaxy; (ii) the spread in the intrinsic ellipticity distribution of the source population; (iii) observational errors arising from uncertainties in the measurement of ellipticities from the images for the faintest objects and (iv) contamination by foreground galaxies mistaken as background. As mentioned in Section 2.2.2, the partitioning of mass into subhaloes and the smooth component as done here is largely independent of the $N(z)$ of background galaxies.

In terms of the total contribution to the error budget, based on simulations we find that the shot-noise is the most significant source of error, amounting to $\sim$50 per cent; followed by the width of the intrinsic ellipticity distribution which contributes $\sim$20 per cent, and the other three sources together contribute $\sim$30 per cent. This elucidates the future strategy for such analyses – going significantly deeper and wider in terms of the field of view is likely to provide considerable gains. Mosaicked ACS images are the ideal data sets for this galaxy–galaxy lensing analyses, and such work is currently in progress.

4 COMPARISON WITH *N*-BODY SIMULATIONS

In this section, we present a comparison between the properties of the subhaloes determined using the lensing analysis detailed above and results from *N*-body simulations. For this study, we make use of the Millennium Simulation, recently carried out by the Virgo Consortium and described in detail in Springel et al. (2005). The simulation follows $N = 2160^3$ particles within a comoving box of size $500\,h^{-1}$ Mpc on a side. With a particle mass of $8.6 \times 10^8\,h^{-1}\,\mathrm{M}_\odot$ and a spatial resolution of $5\,h^{-1}$ kpc, the Millennium Simulation provides an unprecedented combination of high resolution and large volume that allows the formation of rare objects – like massive lensing clusters – to be followed in a representative fashion. It therefore represents an ideal simulation to compare with observations as a relatively large sample of massive, lensing clusters can be extracted over the redshift range probed by the observations. For the 64 time slices produced by the simulation, embedded substructures within dark matter haloes were identified with the algorithm SUBFIND (Springel et al. 2001). In brief, the algorithm decomposes a given particle group (previously identified with a standard friends-of-friends algorithm) into a set of disjoint substructures, each of which is identified as a locally overdense region in the density field of the background halo. After the regions containing substructure candidates have been identified, an unbinding procedure is employed to iteratively reject all particles with positive total energy. All substructures that survive the unbinding procedure, and still have at least 20 self-bound particles, are considered to be genuine substructures. We refer to the original paper for more details on the algorithm. We note however that the identification of subhaloes within haloes represents a difficult technical problem. A variety of different algorithms have been developed in order to accomplish this task (e.g. Gottlöber, Klypin & Kravtsov 1998; Klypin et al. 1999; Springel et al. 2001; Weller et al. 2005), but unfortunately little work has been done so far to compare the properties of subhaloes identified with different methods, so that the systematic effects and differences inherent in these methods are largely unknown.

In order to carry out our comparison with lensing results, we have selected all haloes with $M_{200} \geqslant 8 \times 10^{14}\,\mathrm{M}_\odot$ from the simulation box at the snapshots corresponding to the redshifts of the lensing clusters (see Table 2). We find 17, 15 and 12 very massive haloes at the redshifts of the clusters A 2218, A 2390 and Cl 2244−02, respectively. Massive cluster haloes are on the tail of the mass function in a ΛCDM Universe and their number decreases rapidly with increasing redshift. For Cl 0024+16 and Cl 0054−27, we have therefore combined two adjacent snapshots (in both cases the redshift of the observed clusters lies in between those of the used snapshots), which led to 12 and six candidates, respectively.

For each cluster halo, we have analysed the distribution of the subhalo properties by projecting along the *x*-, *y*- and *z*-axes and keeping subhaloes 2 Mpc from the cluster centre that are projected to within 1 Mpc, identified with the position of the most bound particle. The distributions we discuss in the following are then the average over the three projections of all the haloes identified for each redshift.

4.1 The mass function of substructures

As mentioned in Section 1, a direct mapping of the substructure mass function is ultimately of interest since it provides an important test of the ΛCDM paradigm. In addition, it is intimately connected to the galaxy formation process: comparison of the dark halo mass function with the observed luminosity function of galaxies can provide valuable insights into the physical processes driving galaxy formation and evolution. In this work, we restrict ourselves to a

Table 2. Parameters that define the mass models of the subhaloes for the lensing clusters.

Cluster	z	σ^* (km s^{-1})	r_t^* (kpc)	M_{ap}/L_v ($\mathrm{M}_\odot/\mathrm{L}_\odot$)	M^* ($10^{11}\,\mathrm{M}_\odot$)	σ_{clus} (km s^{-1})	$\rho_{clus}(r=0)$ ($10^6\,\mathrm{M}_\odot$ kpc^{-3})
A 2218	0.17	180 ± 10	40 ± 12	5.8 ± 1.5	$\sim$14	1070 ± 70	3.95
A 2390	0.23	200 ± 15	18 ± 5	A 4.2 ± 1.3	$\sim$6.4	1100 ± 80	16.95
AC 114	0.31	192 ± 35	17 ± 5	6.2 ± 1.4	$\sim$4.9	950 ± 50	9.12
Cl 2244−02	0.33	110 ± 7	55 ± 12	3.2 ± 1.2	$\sim$6.8	600 ± 80	3.52
Cl 0024+16	0.39	125 ± 7	45 ± 5	2.5 ± 1.2	$\sim$6.3	1000 ± 70	3.63
Cl 0054−27	0.57	230 ± 18	20 ± 7	5.2 ± 1.4	$\sim$9.4	1100 ± 100	15.84

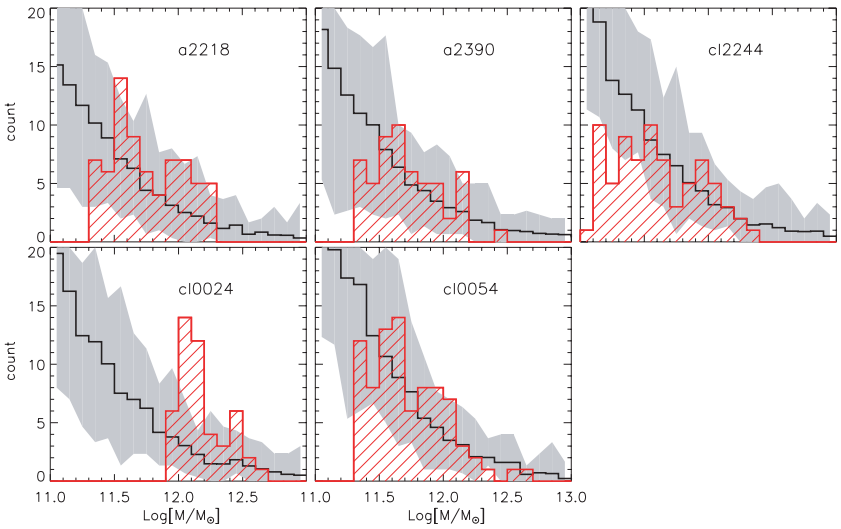

Figure 2. Comparison between substructure mass function retrieved from the galaxy–galaxy lensing analysis (red shaded histograms) and results from haloes selected from the Millennium Simulation. The black solid line in each panel represents the average subhalo mass function of haloes selected at the redshift of the observed lensing cluster (see text for details). The grey shaded region represents, for each value of the subhalo mass, the min–max number of substructures found in the simulated haloes.

comparison of the properties of the dark matter component. A yet more detailed comparison for A 2218 in terms of observable galaxy properties by means of simulations and semi-analytic techniques is presented elsewhere (De Lucia, Natarajan & Springel, in preparation).

In Fig. 2 we compare the substructure mass function retrieved from the galaxy–galaxy lensing analysis (hashed histograms) with the results from the numerical simulation. The black solid line in each panel represents the average over the three orthogonal projections of all the massive haloes identified for each redshift. All subhaloes along the line of sight up to 2 Mpc away from the cluster centre that are projected to within 1 Mpc are included in the inventory. The grey filled histograms show for each value of the subhalo mass, the minimum and maximum number of substructures found in the simulated clusters. The lower mass cut-off for the mass function determined from lensing is set by observational limitations, primarily the accuracy with which anisotropies in the shear field can be statistically detected. We note that the mass of the subhaloes used to build the grey histogram in Fig. 2 is defined in terms of the total number of particles they contain, and *has been multiplied by a correction factor* of 2, as discussed below. As shown in Fig. 1, the error bars in σ_{0*} and r_{t*} retrieved from the lensing observations translate into a factor of 2 error in the aperture mass of substructures.

When taken at face value this correction factor of 2 would signal a discrepancy between the simulation and lensing results. However, we argue that the difference is dominated by systematic effects in the measurement of substructure masses in the simulation, and possibly also in the lensing analysis. Note that the algorithm SUBFIND identifies substructures as overdense regions bounded by an isodensity surface where the density equals the local value of the background host halo. Because of this criterion for identifying substructure, it is possible that our subhalo masses are biased low, because only the 'tip of the iceberg' is seen. This effect should increase the closer a subhalo is located to the centre. We will now show that this suspicion is indeed true.

For our comparison with lensing data, the most important question is whether the self-bound mass reported by SUBFIND for a substructure actually accounts for the *full* mass enhancement present at the location of the substructure in the *N*-body simulation. To determine this mass enhancement, one can measure the enclosed mass within a little sphere around the location of the substructure and subtract from it the mass in the same sphere after spherically averaging the whole mass distribution of the halo around the halo centre. The latter gives an estimate of the background density in the volume occupied by the substructure. If the mass distribution is a superposition of a spherically symmetric background halo and an embedded substructure, then this procedure will (almost exactly) recover the true mass of the substructure independent of the density profile of the background halo and that of the substructure, provided that the spherical aperture fully encloses the substructure. The mass estimate will be biased slightly low because the spherically averaged mass distribution includes the substructure mass, but this should be negligible if the volume of the substructure is small against that of the background halo.

This leaves the question of what to choose for the radius of the sphere that is needed in the measurement. If there was only a single substructure in a spherically symmetric halo, the result would be invariant once the sphere is large enough to fully enclose the substructure. In real-world haloes we will suffer from growing errors in the measurement when the aperture becomes too large, both from other nearby substructures and from the fact that the background halo is not exactly spherical in shape. As a simple compromise we have adopted three times the half-mass radius measured for the substructure (the half-mass radius is the radius that enclosed half the bound particles) to carry out our measurements of the mass enhancements. Note that for an NFW halo, the virial radius would be 2.8 times the half-mass radius for a concentration of 10, while it would be 3.2 times the half-mass radius for a concentration of 15.

Adopting the above measurement procedure, we have determined the mass enhancements $m_{\rm enh}$ around the positions of all substructures identified by SUBFIND in haloes with masses above $10^{14}\,h^{-1}\,{\rm M}_{\odot}$, and with a minimum particle number of 1000 (in total $\sim$31 000 objects).

In Fig. 3, we show the ratio between the measured mass-enhancement and the corresponding SUBFIND self-bound mass as a function of radial position of the substructure within the parent

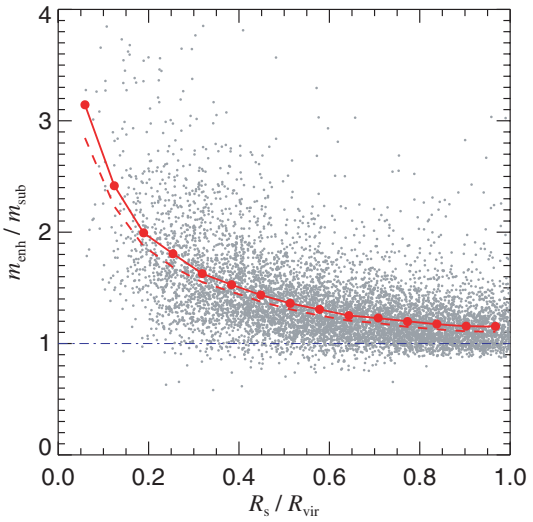

Figure 3. Comparison of the actual mass enhancements found around the locations of substructures (m_{enh}) with the self-bound mass m_{sub} reported by SUBFIND, as a function of radial distance R_s in their parent halo of virial radius R_{vir}. All substructures with more than 1000 particles in haloes above $10^{14}\,h^{-1}\,M_\odot$ in the Millennium Simulation were analysed. A random 25 per cent subsample of the points are included in the scatter diagram. The solid line with symbols gives the mean in each radial bin for the whole sample, while the dashed line is the median in each bin.

halo. There is clearly a mass-bias with a strong radial dependence. The m_{sub} masses reported by SUBFIND for substructures in the inner parts of clusters are systematically biased low; the real mass enhancements relevant for lensing can be a factor of 2–3 higher in the innermost parts of the cluster. For the bulk of the substructures at larger radii, there is only a small difference of the order of ∼20 per cent or so, a value that could also be weakly affected by our choice of aperture radius. However, the radial trend of the mass ratios is robust. While most of the overall substructure mass is found in the outer parts of the cluster, we note that the luminous cluster galaxies are much more centrally concentrated (Springel et al. 2001), so that the bias in the inner parts enters with a large weight in our comparison of lensing data with the *N*-body simulations. This provides the quantitative basis for our fiducial correction factor of 2 that we applied in the comparison shown in Fig. 2. We think a factor of this order is plausible given the systematics of current techniques, but it is also clear that a more precise determination will require an improved understanding of the systematics of both the substructure finder and the lensing analysis.

We note that we have also checked whether there is any mass dependence of this 'bias' in the SUBFIND masses, but we have found no evidence for this. This is consistent with the fact that there is a good uniformity of the measured slopes for the subhalo mass function from different studies (De Lucia et al. 2004; Diemand et al. 2004), which suggests that the systematics of the substructure finders can be accounted for through simple scalefactors, at least at a statistical level. Also, we think that it is likely that other algorithms for identifying substructures suffer from this problem in similar ways.

In addition to the above, is likely that there are some systematic effects in the mass estimate based on the lensing analysis as well. Here a systematic overestimate appears more likely, arising, for example, if the most massive substructures correspond to haloes that have fallen in most recently, as indicated by recent numerical studies (De Lucia et al. 2004; Gao et al. 2004). As for the mass reconstruction technique employed here, biases can also be introduced due to the possible existence of substructure along the line of sight, not in the lens plane but behind it (Natarajan, in preparation). Fig. 2 also shows that there is a large scatter among simulated clusters and since the number of substructures in the observable mass range is quite small, we also expect large system-to-system variations between different observed systems. Besides, as shown in Table 2, the subhalo masses are uncertain to within a factor of 2 from the galaxy–galaxy lensing analysis, based on the observational limitations from current data.

We note here in our preliminary comparison of the lensing derived mass function with that extracted from the simulation of a single, massive cluster (Natarajan & Springel 2004), we had found excellent agreement without the need for a mass correction factor. However, it turns out that this result was influenced by not correctly taking into account the spatial geometry of the *HST* field. When this effect is appropriately included, our present results are consistent with this earlier work, and a mass correction factor of 2 is required to obtain quantitative consistency. Note that this is within the limits of the systematic uncertainties both of the substructure mass detection in the simulations as well as those from the lensing analysis. We appear to be missing subhaloes at the high-mass end ($\log M \geqslant 12.5$), in the lensing determination. This is likely due to the fact that such high-mass haloes probably host more than one luminous component. We plan to investigate this issue further in our detailed study of A2218 in future work.

Overall, it is therefore remarkable that we find very good qualitative agreement in the mass range sampled by the lensing analysis, and very good quantitative agreement as well when the systematic biases are approximately corrected for within the errors. It is interesting to note here that the only obvious outlier is Cl 0024+16. This is the only system that clearly has a bimodal structure with two almost equal mass clumps separated by a small redshift offset. Its bimodal structure has been interpreted as a sign of a recent merger (Czoske et al. 2002). Clearly, if this is indeed the case, the comparison with relaxed massive haloes from the Millennium Simulation is not appropriate. We plan to investigate this question in more detail in future work by comparing the properties of the substructures in Cl 0024+16 with clusters selected from the Millennium Simulation that are recent mergers of equivalent mass.

4.2 The distribution of velocity dispersions

In Fig. 4, we compare the distribution of velocity dispersions retrieved by the lensing analysis and the average distributions obtained for the simulated clusters selected from the Millennium Simulation. The velocity dispersions of substructures in simulated clusters are estimated using the velocity information for all the particles attached to the dark matter substructure and have been scaled by a factor of $\sqrt{2}$ (see previous section). Again we find generally a good agreement over the range sampled by the lensing analysis, except for Cl 0024+16, which yet again appears to be an outlier (see discussion in previous section). Note here that the velocity dispersion retrieved from the lensing analysis is one of the two parameters that characterizes each subhalo. This velocity dispersion is the normalization of the Faber–Jackson relation, therefore, relates the mass (for the PIEMD model) to that of early-type galaxies. For the simulated haloes the measured velocity dispersion is that of the dark matter alone. We note that Springel et al. (2001) used a factor equal to 0.9 to convert the 1D dispersions of subhaloes into stellar velocity dispersions, which was adopted to match the zero-point of the Faber–Jackson relation. Due to the dissipation involved in star formation, it is plausible that the stellar velocity dispersion is *smaller*

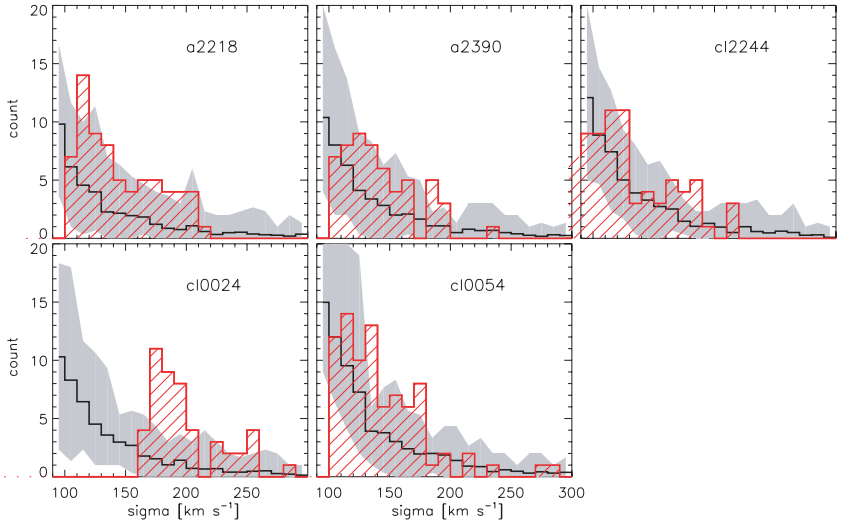

Figure 4. As in Fig. 2 but for the distribution of velocity dispersions.

than that of the dark matter. On the other hand, we argued above that our mass estimates might be biased low. We explore spatial and velocity biases in more detail using the lensing results from A 2218 in a forthcoming paper.

4.3 The distribution function of tidal radii

We use the aperture radii derived from the lensing analysis as a proxy for the tidal radii for the subhaloes. These aperture radii are more compact than the tidally truncated extents of the subhaloes. This radius cannot be identified directly with the tidal radius defined in the usual sense, but is proportional to it. In Fig. 5, we finally show the comparison between the distribution of aperture radii (r_t) retrieved by the lensing analysis with the average distributions of the tidal radii of substructures in simulated clusters selected from the Millennium Simulation. The solid black line in the figure and the grey filled region are obtained by measuring, for each substructure, the radius $r_{\rm half}$ that divides the halo mass in equal inner and outer parts. We note that, by using this measure of the radius, we find a very nice agreement with the distributions retrieved by the lensing analysis (with the usual exception of Cl 0024+16) over the full range sampled by the observations. $r_{\rm half}$, however, represents an underestimate of the 'tidal radius' of a dark matter substructure. The dashed black line in Fig. 5 gives the distribution obtained by using the radius corresponding to the maximum circular velocity ($r_{\rm max}$), which is offset with respect to $r_{\rm half}$ by a factor that is slightly less than 2. We note that, as explained in the previous sections, the mass retrieved by the lensing analysis is essentially the mass within a fixed aperture, which is then identified as being proportional to the tidal radius of the associated dark matter substructure. Given the uncertainty in the measurement technique, the good agreement shown in Fig. 5 is therefore noteworthy. We recall that, in order to obtain a good agreement with the observed subhalo mass function, we have corrected their mass by a factor of 2. We are therefore in a situation where the substructures detected in the simulations are slightly bigger but less massive than those retrieved by our lensing technique. Such a situation would be expected if the density profiles assumed for the substructures are systematically denser in the inner

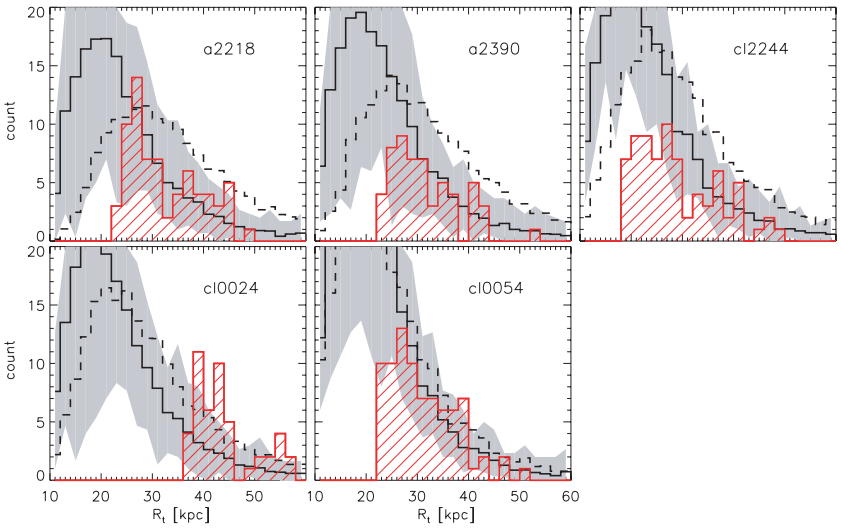

Figure 5. As in Fig. 2 but for the distribution of tidal radii. The solid black line with the grey regions are obtained by measuring for each substructure, the radius corresponding to its half-mass. The dashed black line is obtained by taking the radius corresponding to the maximum circular velocity.

parts than the simulated subhaloes. And, in fact, recent numerical studies suggest that dark matter subhaloes have softer profiles than NFW (Hayashi et al. 2004). Unfortunately our lensing technique is not sensitive to the choice of mass profile, rather it represents a tool to determine the total mass enclosed within an aperture. Higher resolution data will in the future allow the slopes of the mass profiles in substructure to be constrained. Adiabatic contraction of the dark matter density profile in response to the baryonic component in the inner regions of the cluster halo (on scales of $r < 10$–50 kpc) is also expected to be relevant, however the importance and significance remains to be assessed from numerical simulations. There are two conflicting claims on how significant this effect at the present time (Rozo et al. 2006; Zappacosta et al. 2007).

5 CONCLUSIONS AND DISCUSSION

In this paper, we present (i) high-resolution mass models for lensing clusters, (ii) the inferred mass function of subhaloes inside these clusters and (iii) a detailed comparison of the subhalo mass function, the velocity dispersion and aperture radii function with an ensemble of cluster-sized haloes selected from the Millennium Simulation. Detailed results of the application of our galaxy–galaxy lensing analysis techniques to five *HST* cluster lenses are used to construct high-resolution mass models of the inner regions. In order to do so we have utilized both strong and weak lensing observations for these massive clusters. The goal has been to quantify substructure in the cluster assuming that the subhaloes follow the distribution of bright, early-type cluster galaxies. Similar attempts have been made in the lower density field environment yielding typical galaxy masses and central velocity dispersions. The mass distribution for a typical galaxy halo inferred from field studies is extended with no discernible cut-off in most analyses with the exception of one study by Hoekstra et al. (2004) where they report $r_{\rm t} = 260^{+124}_{-73}$ kpc using data from the CNOC-2 fields. By contrast, in the cluster environments probed in this work we detect an edge to the mass distribution in cluster galaxies. We have performed various stringent checks to ascertain that this is not an artefact of the choice of mass model. Rather this result provides evidence for tidal stripping by the global cluster potential well.

Aside from the detailed lens models, we also present the mass spectrum (albeit within a limited mass range with subhalo masses ranging from 10^{11}–$10^{12.5}\,{\rm M}_{\odot}$) of substructure in the inner regions of these clusters. The survival and evolution of substructure offers a stringent test of structure formation models within the CDM paradigm. Subhaloes of the scale detected in all these clusters indicate a significant probability of galaxy–galaxy collisions over a Hubble time within a rich cluster. However, since the internal velocity dispersions of these clumps associated with early-type cluster galaxies ($\sim$150–250 km s^{-1}) are much smaller than their orbital velocities, these interactions are unlikely to lead to mergers, suggesting that the encounters of the kind simulated in the galaxy harassment picture by Moore et al. (1996) are the most frequent and likely. High-resolution cosmological *N*-body simulations of cluster formation and evolution (Moore et al. 1996; Ghigna et al. 1998; De Lucia et al. 2004), find that the dominant interactions are between the global cluster tidal field and individual galaxies after $z = 2$. The cluster tidal field tidally strips galaxy haloes in the inner 0.5 Mpc efficiently and the radial extent of the surviving haloes is a strong function of their distance from the cluster centre. Much of this modification is found to occur between $z = 0$ and 0.5.

We have performed a detailed comparison of the subhalo mass function, velocity dispersion function and the distribution of aperture radii retrieved from lensing with an ensemble of massive clusters from the Millennium Simulation, which provides an ideal data set for such an analysis. A series of systematic effects, due to the algorithm used to identify substructures in the simulation, needs to be taken into account when performing such a comparison. In addition, it should be kept in mind that the level of uncertainty of the observational results is still relatively high (e.g. the mass derived from lensing is only accurate to within a factor of 2 and the technique is not sensitive to the choice of the substructure mass profile). Overall, we find consistency between the distribution of substructure properties retrieved using the lensing analysis and those obtained from simulations, although our detailed comparison seems to suggest that simulated substructures are slightly bigger but less massive than subclumps detected by means of lensing techniques. This might be due to systematic differences between the density profiles of simulated substructures and those assumed in the lensing model. Unfortunately, the technique is not sensitive to this choice but higher resolution data will allow in the future the slopes of the mass profiles in substructures to be constrained.

Despite the uncertainties mentioned above, the general agreement between simulations and results determined *independently* from lensing is remarkable. Our work represents a powerful test of the ΛCDM model, which at present appears to be consistent with the amount of observed substructure in massive, lensing clusters, up to redshifts of $\sim$0.6, given the uncertainties. It will be very interesting to tighten the constraints with future lensing data.

ACKNOWLEDGMENTS

The authors acknowledge Simon White for support and encouragement throughout this project. PN is grateful to the Virgo Consortium for access to the Millennium Simulation data. She acknowledges support from NASA via *HST* grant HST-GO-09722.06-A. She also thanks her collaborators Jean-Paul Kneib, Ian Smail and Richard Ellis for help with the observational data and useful input on the work. GDL thanks the Alexander von Humboldt Foundation, the Federal Ministry of Education and Research, and the Programme for Investment in the Future (ZIP) of the German Government for financial support.

REFERENCES

Aldering G. et al., 2003, SPIE, 4835, 40, preprint (astro-ph/0209550)
Benson A. J., Frenk C. S., Lacey C. G., Baugh C. M., Cole S., 2002, MNRAS, 333, 177
Brainerd T., Blandford R., Smail I., 1996, ApJ, 466, 623
Bruzual G., Charlot S., 2003, MNRAS, 344, 1000
Bullock J. S., Kravtsov A. V., Weinberg D. H., 2000, ApJ, 539, 517
Clowe D., Scheider P., 2002, A&A, 395, 385
Couch W. J., Barger A. J., Smail I., Ellis R. S., Sharples R. M., 1998, ApJ, 497, 188
Czoske O., Moore B., Kneib J., Soucail G., 2002, A&A, 386, 31
De Lucia G., Kauffmann G., Springel V., White S. D. M., Lanzoni B., Stoehr F., Tormen G., Yoshida N., 2004, MNRAS, 348, 333
Diemand J. et al., 2004, MNRAS, 352, 535
Farouki R., Shapiro S. L., 1981, ApJ, 243, 32
Gao L., De Lucia G., White S. D. M., Jenkins A., 2004, MNRAS, 532, L1
Ghigna S., Moore B., Governato F., Lake G., Quinn T., Stadel J., 1998, MNRAS, 300, 146
Gottlöber S., Klypin A. A., Kravtsov A. V., 1998, in Evolution of Large-scale Structure: From Recombination to Garching, preprint (astro-ph/9810191)
Griffiths R. E. et al., 1994, ApJ, 435, L19
Guzik J., Seljak U., 2002, MNRAS, 335, 311

Hayashi E. et al., 2004, MNRAS, 355, 794
Hoekstra H., Yee H. K., Gladders M., 2004, ApJ, 606, 67
Hudson M. J., Gwyn S. D. J., Dahle H., Kaiser N., 1998, ApJ, 503, 531
Kassiola A., Kovner I., 1993, ApJ, 417, 474
Kleinheinrich M. et al., 2005, A&A, 439, 513
Klypin A., Kravtsov A. V., Valenzuela O., Prada F., 1999, ApJ, 522, 82
Kneib J.-P., 1993, PhD thesis, Univ. Paul Sabatier, Toulouse
Kneib J., Ellis R. S., Couch W., Smail I. R., Sharples R., 1996, 471, 643
Kneib J. et al., 2003, ApJ, 598, 804
Kravtsov A. V., Gnedin O. Y., Klypin A. A., 2004, ApJ, 609, 482
Le Fevre O. et al., 2004, A&A, 417, 839
Limousin M., Kneib J., Natarajan P., 2005, MNRAS, 356, 309
Limousin M. et al. 2006, MNRAS, submitted
Maller A., Bullock J., 2004, MNRAS, 355, 694
Merritt D., 1983, ApJ, 264, 24
McKay T. et al., 2002, ApJ, 571, L85
Moore B., Katz N., Lake G., Dressler A., Oemler A., 1996, Nat, 379, 613
Moore B., Ghigna S., Governato F., Lake G., Quinn T., Stadel J., Tozzi P., 1999, ApJ, 524, L19
Natarajan P., Kneib J.-P., 1997, MNRAS, 287, 833
Natarajan P., Springel V., 2004, ApJ, 617, L13
Natarajan P., Kneib J., Smail I., Ellis R. S., 1998, ApJ, 499, 600
Natarajan P., Kneib J., Smail I., 2002a, ApJ, 580, L11
Natarajan P., Loeb A., Kneib J., Smail I., 2002b, ApJ, 580, L17
Okamoto T., Habe A., 1999, ApJ, 516, 591
Ota N., Mitsuda K., Fukazawa Y., 1998, ApJ, 495, 170
Richstone D., 1976, ApJ, 204, 642
Rozo E., Nagai D., Keeton C., Kravtsov A., 2006, preprint (astro-ph/0609621)
Schneider P., Rix H., 1997, ApJ, 474, 25
Sheldon E. et al., 2004, A&A, 127, 2544
Spergel D., Steinhardt P. J., 2000, Phys. Rev. Lett., 84, 17, 3760
Springel V., White S. D. M., Tormen G., Kauffman G., 2001, MNRAS, 328, 726
Springel V. et al., 2005, Nat, 435, 629
Tyson J. A., Kochanski G., De'll Antonio I. P., 1998, ApJ, 498, L107
Weller J., Ostriker J., Bode P., Shaw L., 2005, MNRAS, 364, 283
Wolf C. et al., 2004, A&A, 421, 913
Wilson G., Kaiser N., Luppino G. A., Cowie L. L., 2001, ApJ, 555, 572
Zappacosta L. et al., 2007, ApJ, in press (astro-ph/0602613)
Ziegler B., Bower R. G., Smail I., Davies R. L., Lee D., 2001, MNRAS, 325, 157

This paper has been typeset from a TEX/LATEX file prepared by the author.